Host–Guest Interactions and Transport Mechanism in Poly(vinylidene fluoride)-Based Quasi-Solid Electrolytes for Lithium Metal Batteries

Nicholas Vallana[a, b], Eleonora Carena[a, b], Nicole Ceribelli[a], Lorenzo Mezzomo[a, b], Giovanni Di Liberto[a], Michele Mauri[a], Chiara Ferrara[a, b], Roberto Lorenzi[a], Livia Giordano[a, b], Riccardo Ruffo[a, b], Piercarlo Mustarelli[a, b,*]

a Department of Materials Science of University of Milano Bicocca, Via Cozzi 55, 20125 Milano, Italy.
b GISEL-INSTM, Unit of Milano Bicocca, Via Cozzi 55, 20125 Milano, Italy.

*Corresponding author: piercarlo.mustarelli@unimib.it

Abstract

All-solid-state lithium metal batteries (SS-LMBs) are expected to meet the strong requirements of the automotive sector in terms of performance and safety. Among the different solid electrolytes, poly(vinylidene fluoride) (PVDF)-based systems offer good performance in terms of ionic conductivity and stability at the anodic interface. However, despite the high polymer permittivity (ε′ ≈ 10–11) which should allow efficient salt dissociation, there is growing evidence that the ionic transport requires the presence of a non-negligible amount of residual, or permanent, solvent in the membrane. In this paper, we study the Li^+ transport mechanism in a model system consisting of poly(vinylidene fluoride-*co*-hexafluoropropylene) (PFDF-HFP), lithium bis(fluorosulfonyl)imide (LiFSI) salt, and dimethylformamide (DMF) as permanent solvent, combining a large set of experimental techniques (thermal analysis, NMR, IR and Raman spectroscopy, impedance spectroscopy) and accurate density functional theory (DFT) modeling. We show that Li^+–DMF interactions are predominant in these quasi-solid electrolytes (QSEs) and are the basis of the effective ion transport mechanism. Permanent solvent amounts on the order of $[DMF]/[Li^+] \sim 2–3$ are required to make QSEs able to practically work in a real environment.

Keywords

lithium metal batteries; solid-state electrolyte; solvent; spectroscopy; DFT; transport mechanisms

1. Introduction

Batteries have characterized the development of modern society in the last decades. Today, the battery market for portable electronics and automotive is dominated by lithium-ion batteries, LIBs, which contain organic liquid electrolytes and pose relevant safety issues. (1,2) The need for higher safety and better performance calls for lithium metal as the anode, high-voltage oxides as cathode materials, and solid-state electrolytes. (3,4) In fact, lithium metal has a specific capacity about 1 order of magnitude higher than graphite (3860 vs 372 mAh g^{-1}), but it makes the electrochemical cell more unstable, as lithium dendrites can grow from the anode surface and pierce the electrolyte, so reaching the cathode and leading to short circuit. (5−7) Therefore, the electrolyte must be able to avoid or limit dendrites growth. (8) To this aim, ceramic, polymers, composites, and organic–inorganic hybrids can be exploited. (9) To be used in batteries, solid electrolytes must have conductivity values higher than 10^{-4} S cm^{-1} at room temperature, wide chemical and electrochemical stability, good processability, and high elastic modulus to block dendrites growth. (10) At the same time, they must allow the formation of a stable solid electrolyte interface (SEI). (11,12)

Indeed, among the possible solutions, an interesting class of ion conductors is that of solid polymer electrolytes (SPEs), (13) where a polymer is used both as a physical separator and as a medium to enable the transport of lithium ions. Although poly(ethylene oxide) (PEO) has long been the most studied polymer due to its ability to complex the Li ion and to favor its transport assisted by the cooperative motion of the polymer chains in the amorphous phase, (14−16) in the last years, poly(vinylidene fluoride) (PVDF) and poly(vinylidene fluoride-*co*-hexafluoropropylene) (PVDF-HFP) copolymers emerged as a good alternative because of their outstanding mechanical properties, wide electrochemical stability, and high thermal stability. (17−20) Although in the past decades the attention was chiefly devoted to gel-type electrolytes with liquid content larger than 50 wt %, (21,22) more recently, the focus has been placed on solid-type electrolytes which showed excellent electrochemical characteristics in cells with a lithium metal anode. (23−25) The excellent electrochemical properties of PVDF-based systems, including organic-modified polymers, blends, and composites, were recently reviewed by Zhou et al. (26) Even if the physical nature of these systems resembles that of a solid, it was shown that the ions transport in these electrolytes is favored/assisted by residual solvent (e.g., dimethylformamide, DMF) trapped inside the polymer matrix after casting. (23−25) However, there is still a strong debate about the role played by the residual solvent, “permanent” in the following, in these quasi-solid electrolytes (QSEs).

In this study, we performed a thorough and careful analysis of the effects of permanent solvent on the functional properties of PVDF-HFP-based electrolytes, also to shed light on the mechanism underlying ion transport in these new QSEs. By means of a careful experimental-computational approach, which includes thermal and mechanical analysis, microscopy, several spectroscopies, and density functional theory (DFT) modeling, we showed that a solvent concentration $[DMF]/[Li^+] \sim 2–3$ is needed to ensure good ionic conductivity and to allow full electrolyte operation. We also showed that the electrostatic interactions between the salt and the solvent are predominant with respect to those between salt and polymer, despite the high permittivity of the polymer itself.

2. Experimental Section

2.1. Membrane Fabrication

The electrolyte membranes were prepared by solvent casting. The solvent was a 7:3 v/v mixture of tetrahydrofuran (THF) (Alfa Aesar, anhydrous, 99.8+ %, boiling point 66 °C) and dimethylformamide (DMF) (Alfa Aesar, anhydrous, 99.8%, boiling point 153 °C). The solute (5 wt % concentration) was made of PVDF-HFP Kynar 2751 (Arkema) and lithium bis(fluorosulfonylimide) (LiFSI) (Solvionic, 99.9% purity), in a 3:2 weight ratio. The chemicals were stored in a glovebox (MBraun, <0.1 ppm of H_2O and O_2) and used as received. The solutions were then poured into circular PTFE molds (7 mL of solutions in a mold of 5 cm in diameter). For some analyses, polymer membranes without lithium salt were prepared in the same way.

The QSEs properties were evaluated both vs the solvent composition and the drying procedure to which the cast membranes were subjected. Besides the THF/DMF 7:3 v/v mixture, we investigated electrolyte membranes prepared with pure THF, pure DMF, and with a solution where the amount of DMF is the smallest possible reported to be able to remain complexed within the structure, knowing that the solvation number of DMF per lithium-ion is 3.29. (24) This mixture of THF and DMF, with DMF at 2.6% in volume, was called "permanent DMF" or simply "PERM". Concerning the drying protocol, samples were compared both at different days of drying and after a final vacuum treatment to remove the remaining solvent as much as possible. The samples were labeled using the following protocol: A_BBB(_CC), where A refers to the composition of the sample (P for the polymer powder, M for the polymer membrane, and E for the electrolyte also comprising Li salt), BBB is related to the casting solution (7:3 for the 7:3 v/v THF:DMF mixture, PERM, THF, and DMF), and CC describes the drying procedure specifying both the time, S for short (3 days) and L for long (7 days), and the presence of one or more vacuum treatments (+V, + 2 V). The compositions of the different samples are reported in Table 1.

Table 1. Composition and Quantities Used in the Preparation of Electrolyte Solutions: (a) specific amount and (b) percent amount for each component used in the preparation of the solutions; (c) excess in mass of the final membranes after casting, which is attributed to residual solvent for the samples after short drying; (d) long drying; and (e) after the vacuum treatments

(a)

sample	total volume (mL)	volume of DMF (%)	mass of DMF (g)	volume of THF (%)	mass of THF (g)	total amount of solvent (g)	mass of PVDF (g)	mass of LiFSI (g)	total mass of sample (g)
E_7:3	7	30	1.982	70	4.312	6.294	0.200	0.133	6.627
E_DMF	7	100	6.608	0	0	6.608	0.200	0.133	6.941
E_PERM	7	2.6	0.172	97.4	6.000	6.172	0.200	0.133	6.505
E_THF	7	0	0	100	6.160	6.160	0.200	0.133	6.493

(b)

sample	mass of DMF (%)	mass of THF (%)	mass of PVDF (%)	mass of LiFSI (%)
E_7:3	29.92	65.08	3.00	2.00
E_DMF	95.20	0	2.88	1.92
E_PERM	2.64	92.24	3.07	2.04
E_THF	0	94.87	3.08	2.05

(c)

sample	mass of solute (g)	total mass of casting solution (g)	mass after short drying s" (g)	excess in mass (g)	excess in mass (%)	moles of residual DMF (mmol)	[DMF]/[Li^+] mol/mol
E_7:3	0.333 ± 0.002	6.627 ± 0.004	0.452 ± 0.010	0.119 ± 0.012	26.4 ± 2.2	1.63 ± 0.16	2.29 ± 0.09
E_DMF	0.333 ± 0.002	6.941 ± 0.003	0.467 ± 0.007	0.134 ± 0.009	28.7 ± 1.6	1.83 ± 0.12	2.58 ± 0.06
E_PERM	0.333 ± 0.002	6.505 ± 0.004	0.435 ± 0.011	0.102 ± 0.013	23.5 ± 2.4	1.40 ± 0.18	1.96 ± 0.12
E_THF	0.333 ± 0.002	6.493 ± 0.003	0.343 ± 0.002	0.010 ± 0.003	2.9 ± 0.4		

(d)

sample	mass after long drying "L" (g)	excess in mass (g)	excess in mass (%)	moles of residual DMF (mmol)	[dmf]/[Li^+] mol/mol
E_7:3	0.383 ± 0.007	0.050 ± 0.009	15.0 ± 1.6	0.68 ± 0.12	0.96 ± 0.06
E_DMF	0.392 ± 0.005	0.059 ± 0.007	17.7 ± 1.2	0.81 ± 0.09	1.13 ± 0.04
E_PERM	0.380 ± 0.08	0.047 ± 0.010	14.1 ± 1.8	0.64 ± 0.14	0.90 ± 0.08
E_THF	0.341 ± 0.002	0.008 ± 0.003	2.4 ± 0.4		

(e)

sample	mass after vacuum treatment "+V" (g)	excess in mass (g)	excess in mass (%)	moles of residual DMF (mmol)	[dmf]/[Li^+] mol/mol
E_7:3	0.350 ± 0.003	0.017 ± 0.005	5.1 ± 0.8	0.23 ± 0.09	0.33 ± 0.04
E_DMF	0.351 ± 0.002	0.018 ± 0.004	5.4 ± 0.6	0.25 ± 0.06	0.35 ± 0.03
E_PERM	0.349 ± 0.003	0.016 ± 0.005	4.8 ± 0.8	0.22 ± 0.08	0.31 ± 0.04
E_THF	0.339 ± 0.002	0.006 ± 0.004	1.8 ± 0.6		

2.2. Membrane Characterization

2.2.1. ATR-FTIR

The spectra were acquired using a Jasco FT/IR-4100 spectrophotometer from 4000 to 550 cm^{-1} with a resolution of 4 cm^{-1}. For subsequent analysis, we focused on the area of the spectrum from 640 to 690 cm^{-1}, the region where the DMF peaks are located.

2.2.2. Raman

Micro-Raman measurements were recorded at room temperature using a LabRAM confocal spectrometer (Horiba Jobin-Yvon) equipped with a He–Ne laser operating at 632.8 nm in a backscattering configuration. The scattered light was collected by a 50× long working distance objective with a numerical aperture of 0.60 mounted on a microscope head (Olympus BX40) and detected by a charge-coupled device (CCD-Sincerity, Jobin-Yvon) with a resolution of 1 cm^{-1}. The spectral position of the detection system was calibrated with a 521 cm^{-1} Raman line of crystalline silicon as a standard. This was done before each measurement. Reference Raman spectra collected on ionic liquids were measured from sealed glass vials prepared in a glovebox. The membrane sample was measured in air.

2.2.3. Solid-State Nuclear Magnetic Resonance (ssNMR)

^{13}C MAS NMR spectra with high power proton decoupling were collected on a 9.4 T magnet (400 MHz) Bruker Avance III spectrometer equipped with a 4 mm probe (10 kHz spinning speed), by averaging over 1 k scans, with a 90° pulse of 2.5 μs, and delay of 50 s. The spectra were referenced to adamantane as a secondary standard.

2.2.4. NMR Relaxometry

Time Domain NMR, consisting of the acquisition and analysis of ^{1}H NMR free induction decay (FID) after appropriate pulse sequences, was performed with a Bruker Minispec mq20 system. The Minispec is equipped with a BVT3000 nitrogen-fed gas temperature control unit, keeping the sample temperature within 0.1 °C of the set point.

2.2.5. Scanning Electron Microscopy (SEM)

Cross section measurements were made by supporting aliquots of the membranes on conductive silicon pieces with carbon tape to have the cross section exposed to the microscope beam. These measures were made using an SEM-FEG Gemini 500 Zeiss microscope, with a voltage of 5 kV and magnifications of 1000× and 5000×.

2.2.6. Thermogravimetry (TGA)

The thermal properties were evaluated by TGA (Mettler Toledo TGA/DSC 1 STAR System) both vs temperature and under isothermal conditions. TGA experiments vs temperature were carried out by heating from 30 to 250 °C, with a heat rate of 5 °C/min, under nitrogen flux (50 mL min^{-1}). TGAs in isothermal conditions were performed at 150 °C for 9 h with a heat rate of 5 °C min^{-1}, under nitrogen flux as above.

2.2.7. Electrochemical Impedance Spectroscopy (EIS)

The ionic conductivity of the electrolytes was measured by electrochemical impedance spectroscopy (EIS) on symmetric cells using stainless steel (SS) electrodes, with a 1.6 cm (diameter) membrane disc as the electrolyte, in an SS/electrolyte/SS CR2032 coin cell. The measurements were performed in the temperature range from 20 to 90 °C, and in the frequency range from 1 MHz to 100 Hz using a SP-150 potentiostat (Biologic) with a voltage amplitude of 20 mV. The ionic conductivity, σ, was obtained by the relationship

$$\sigma = \frac{1}{R} * \frac{l}{s} \quad \textbf{(1)}$$

where *R* is the resistance obtained by the EIS Nyquist plot, *l* is the thickness of the membrane, and *s* is its contact area. The activation energy, E_a, values of the electrolyte membranes were calculated by means of the Arrhenius equation

$$\sigma = \sigma_0 * e^{-E_a/R'T} \quad \textbf{(2)}$$

where *R*′ is the gas constant.

2.3. Computational Details

The interaction of Li^+ with DMF molecules, FSI^- anions, and PVDF chains was computed by density functional theory (DFT) with the Gaussian16 suite. (27) Geometry optimizations were performed at the B3LYP/6-31G(d,p) level of theory. We used a conductor-like polarizable continuum model (CPCM) (28,29) to account for solvation effects, with a dielectric constant ε = 10.1, close to the one of PVDF. PVDF was simulated by chains containing 15 carbon atoms terminated by methyl groups ($C_{15}F_{14}H_{18}$), derived from α-phase of PVDF, which

guarantees a C/Li^+ ratio close to the experimental formulation. PVDF was used instead of PVDF-HFP for the sake of simplicity, provided that HFP is 6 mol %.

The binding energy of $Li(FSI^-)_p(DMF)_n(PVDF)_m^+$ complexes is defined as the energy involved in the reaction

$$Li^+ + pFSI^- + nDMF + mPVDF \rightarrow Li(FSI^-)_p(DMF)_n(PVDF)_m^+$$

$\Delta E = E(Li(FSI^-)_p(DMF)_n(PVDF)_m^+) - E(Li^+) - pE(FSI^-) - nE(DMF) - mE(PVDF)$, where p and n are the number of FSI^- anions and DMF molecules, respectively, and m is the number of PVDF oligomers surrounding the cation.

Simulated Raman and infrared spectra of the optimized molecular structures of DMF, FSI^-, PVDF, and their Li^+ complexes in the implicit solvent were obtained from the computed vibrational frequencies using a Lorentzian bandwidth of 10 cm^{-1} with the program Molden. (30)

3. Results and Discussion

3.1. Physico Chemical Characterization

3.1.1. ATR-FTIR Spectroscopy

We start our analysis in a qualitative fashion, by using ATR-FTIR spectroscopy, which is a useful tool to investigate the role of solvent in the polymer matrices. DMF as a free solvent ("free-DMF" in the following) shows a peak between 665 and 655 cm^{-1}. In contrast, DMF complexed by the electrolyte ions, presumably Li^+, but in principle, we cannot exclude FSI^-, ("bound-DMF" in the following), shows a peak between 670 and 685 cm^{-1}. (24,31) It should be remembered that THF has a higher volatility and a lower ability to interact with the other matrix components. In fact, our preliminary ^{13}C MAS NMR analyses did not show any significant presence of peaks attributable to THF (see Figure S1) in agreement with the literature. (8,9)

Figure 1 reports the IR spectra under different conditions. As a first analysis, we compared the pure polymer with M_7:3_S and E_7:3_S dried in argon at room temperature. The sample P did not show peaks in the area where the DMF signals occur. The spectrum of M_7:3_S shows a small baseline deflection centered in the free-DMF region. This points to the presence of some residual DMF after drying. In contrast, the spectrum of E_7:3_S shows two well-defined overlapping peaks, one in the "bound-DMF" area and one in the "free-DMF" area, indicating that the presence of salt, likely lithium ions, somehow retains DMF into the polymer as both free and bound moieties. This result is qualitatively confirmed by solid-state NMR (see Figure S2) and quantitatively by Raman (see below) and will be further discussed with the help of DFT modeling.

Figure 1

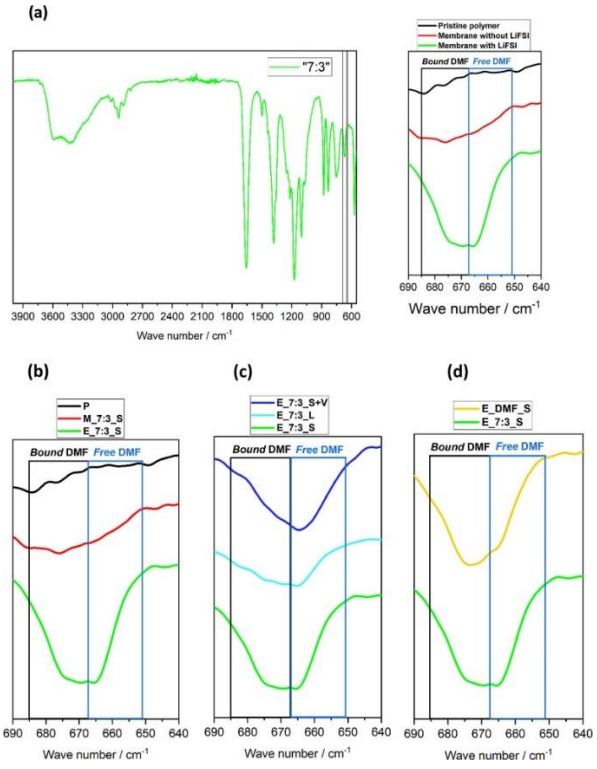

Figure 1. (a) Complete ATR-FTIR spectrum of E_7:3_S. The vertical black lines indicate the spectral region expanded in the right panel. Comparisons of the DMF peaks of panel (a) right vs (b) the presence of the lithium salt; (c) method of drying; (d) solvent mixture. The pristine polymer is also labeled "P".

Figure 1c shows the effects of increasing drying time, even under vacuum, on the quantity of residual DMF. Comparing the spectrum of E_7:3_S with E_7:3_L, the intensity of both peaks decreases. The spectrum of the sample E_7:3_S+V shows a smaller decrease of the signal intensity compared to the sample E_7:3_L.

Finally, Figure 1d compares the IR spectra of E_7:3_S and E_DMF_S. These spectra show how, using only DMF, a greater fraction of it appears to be bound rather than free. This points toward a competitive, albeit small, role of THF in complexing Li^+ ions.

3.1.2. Scanning Electron Microscopy

The SEM images of the samples of interest are reported in Figure S3. The sample E_7:3_S showed a compact and dense layer on the micron scale. The sample E_7:3_L showed a less uniform structure with roughness and holes on a submicron scale. Finally, the sample E_7:3_S+V displayed a well-defined porous structure on a dimensional scale of the order of a few micrometers, probably induced by the removal of the residual DMF through the drying procedure. As we shall see, the weight loss behavior in TGA measurements is strongly dependent on the microstructure of the samples.

3.1.3. Thermogravimetry

More quantitative information about the thermal stability of the membrane and the role played by the solvent mixture can be obtained by TGA. Figure 2a shows the thermograms of the samples P, M_7:3_S, E_7:3_S and E_7:3_L. The samples P and M_7:3_S did not show any mass loss up to 250 °C; this confirms that without the presence of the lithium salt, no solvent remains inside the membranes, in agreement with the ATR-FTIR results. The thermograms of samples E_7:3_S and E_7:3_L showed a more complex behavior with two weight losses (roughly below 100 °C and between 100 and 200 °C) separated by a plateau, which is more evident in the sample dried for a longer time. The weight loss continued, albeit with a lesser slope, up to 250 °C where the measurements were interrupted. At that final temperature, the two samples showed losses of 22 and 14%, respectively. In our previous paper, (32) we erroneously attributed the first loss to THF and the second one to DMF because of their different boiling points. A more careful analysis here revealed that the loss mechanism is somehow governed by the presence of the salt and, at least as a first approximation, is independent of the nature of the solvent. In fact, Figure S4a shows the TGA curves of E_THF_S, E_DMF_S, and E_7:3_S. Even in the case of single solvent, we observed a two-step loss. Therefore, the mass losses of the samples should not simply be related to solvent evaporation, but they contain a contribution from salt degradation. (33)

Figure 2

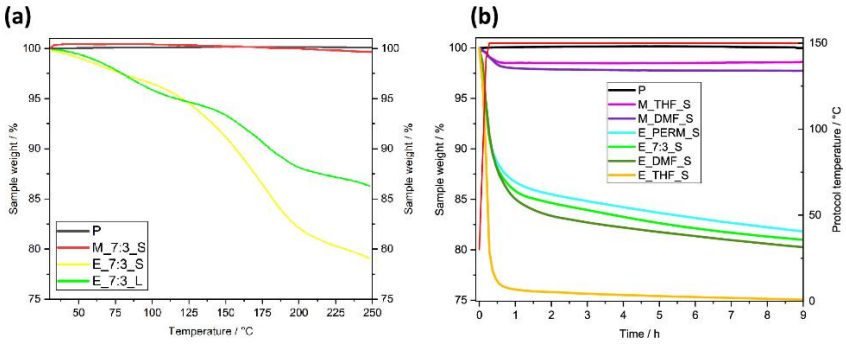

Figure 2. (a) TGA curves vs temperature and (b) TGA isotherms at 190 °C (the red line corresponds to the temperature protocol).

Undoubtedly, also the morphology of the sample plays an important role in determining the trend of the loss process observed in TGA. Figure S4b compares the trends of E_7:3_S, E_7:3_L, E_7:3_S+V, and E_7:3_L+V. The loss of the vacuum-treated samples has a monotonous trend, without showing the steps previously observed. This strong influence of morphology makes it more difficult to address the TGA losses. Moreover, we must consider that LiFSI is highly hygroscopic, and therefore, we cannot exclude the presence of water due to the preparation phases of the TGA measurement, which can further catalyze the degradation of the system. The thermogram of the salt alone is reported in Figure S5: we observed an initial weight loss of ∼2.5% due to absorbed water, followed by salt decomposition at ∼190 °C.

Since the weight loss is linked both to the loss of solvent and to the degradation of the salt, it is not easy to obtain direct information on the permanent amount of solvent as a function of drying. Further information can be obtained through TGA isotherms performed at 150 °C, i.e., close to the boiling temperature of the high boiling solvent (DMF) and sufficiently far from the degradation temperature of the salt ($T \approx 180$ °C; see Figure S5). Figure 2b shows the isotherms of the several samples. P did not reveal any loss after 9 h. The membranes prepared without salt showed a loss of the order of 2%, which is likely due to absorbed water. Again, the addition of salt made the situation more complex: E_7:3_S and E_PERM_S showed losses of the order of 17%, and a similar valuer was obtained for E_DMF_S.

Interestingly, the membrane prepared only with THF showed the largest loss (25%). Indeed, this loss cannot be due only to solvent spillage due to high THF volatility, also considering the much smaller excess in mass present in the membranes after casting (Table 1c). These results confirmed that the weight loss observed by TGA is not simply due to solvent evaporation alone but also to the degradation of the sample. (34) As a rough estimation, assuming that THF is eliminated during drying, we can conclude that a quantity of the order of 20 wt % of DMF is retained in the E_7:3_S and that it is reduced to about 10 wt % after long drying, in reasonable agreement with the data of Table 1. However, the amount of permanently entrapped solvent will significantly affect the transport properties of the QSEs, as shown below.

3.2. Quantitative Investigation of Polymer–Solvent–Salt Interactions

3.2.1. Raman Spectroscopy

To better understand the Li^+ environment and to quantify the ratio between free and bound molecules, we conducted careful Raman investigations focusing on sample E_7:3_S. The Raman spectra in the range 600–1000 cm^{-1} are reported in Figure 3a (the overall Raman spectra are reported in Figure S6). As already evidenced by NMR measurements, Raman experiments confirm the effectiveness of the drying process. In fact, there are no traces of residual THF, which should show an intense peak at 913 cm^{-1} due to ring breathing mode. (35) Accordingly, Raman spectra exhibit signals from only three components: DMF, FSI^-, and minor contributions were from PVDF-HFP. DMF and FSI^- spectra agree with literature data (36,37) and our DFT modeling as shown below, while PVDF-HFP related peaks are found in the region 780–820 cm^{-1}, corresponding to C–F side-chain stretching modes. (38)

Figure 3

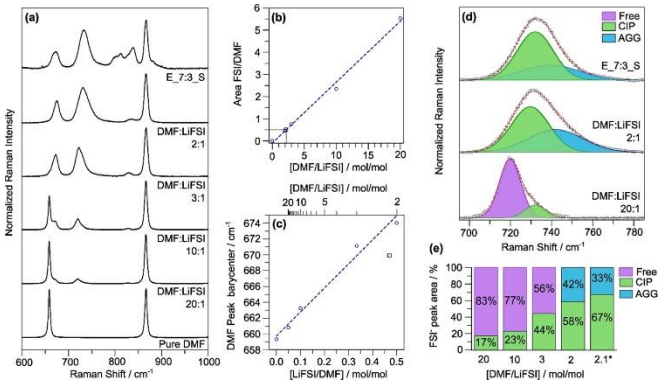

Figure 3. (a) Raman spectra collected on reference solutions of LiFSI in DMF and on sample E_7:3_S; (b) calibration curve (blue empty circles and line) obtained from reference solutions and used to reconstruct the actual concentration of FSI in sample E_7:3_S (black empty square); (c) DMF peak barycenter vs LiFSI/DMF concentration; (d) Gaussian decomposition of the main FSI peak into the three main anion configurations (Free; CIP, contact ion pairs; AGG, aggregates) for the sample E_7:3_S and for the reference solutions with the lowest and the highest concentrations; (e) peak area analysis of all of the spectra according to the spectral decomposition given in (d).

The first step was to use Raman spectroscopy to determine the actual molar ratio of FSI^- to DMF in the membrane after it had dried, as reported in Figure 3b. This was performed by constructing a calibration curve starting from solutions of known concentrations of DMF and LiFSI and assessing the concentration of the species by looking at their characteristic signals. Specifically, the amount of DMF was estimated by the area, I_{DMF}, of the main peak at 865 cm^{-1} ascribable to the C–N–C symmetric stretching, (39) whereas for LiFSI, we monitored the integrated intensity, I_{FSI}, of the band at 720–740 cm^{-1} which is related to the S–N–S symmetric stretching mode. (40) The calibration curve was then constructed by plotting I_{DMF}/I_{FSI} as a function of the nominal DMF/LiFSI mol/mol concentration of the solutions. The I_{DMF}/I_{FSI} ratio was then calculated from the Raman spectrum of sample E_7:3_S, from which the actual concentration was extrapolated using the calibration curve parameters. The DMF/FSI^- turns out to be 2.1 ± 0.2 mol/mol. After the determination of the exact concentrations of DMF and FSI^-, we investigated the effect of the solvation of the Li atoms. The interaction with DMF, similar to the IR-active mode, was monitored by studying the peak at about 660 cm^{-1}. This peak is originated by the O═C–N deformation vibration (41) and, as confirmed by our DFT calculations, it is extremely responsive to the type and number of solvated species. (42,43) As reported in Figure 3a, free-DMF is characterized by a single band centered at 660 cm^{-1}, but as the solute concentration increases, an apparent shift of the peak to higher wavenumbers is observed. The origin of this apparent shift is the presence of a new spectral component attributable to the bound form of the solvent, which is centered at a slightly higher frequency. The fitting of this band into just two components is not trivial, probably due to the presence of different forms of solvating geometries. (43) To reconstruct the solvent behavior in the membrane, we therefore evaluated the position of the band barycenter as a function of solute concentration, avoiding any assumptions about the shape and number of underlying peaks. The result is reported in Figure 3c, where the band position is reported against the measured DMF:FSI^- ratio. For the reference solution, data can be reduced by a straight line passing from 659 cm^{-1} for the pure solvent (completely free DMF) to 674 cm^{-1} for the most concentrated solution corresponding to a molar ratio of FSI^-/DMF of 0.5 (almost completely bound DMF). The barycenter of the band for the sample E_7:3_S is located at 670 cm^{-1}, which corresponds to

an "effective" DMF/FSI^- ratio ~3, quite near to the 2.1 ± 0.2 mol/mol obtained from I_{DMF}/I_{FSI} ratio. This calls just for a relatively small "shielding" role played by the polymer strands, in agreement with the DFT results (see below).

The same approach was adopted to study coordination by the FSI anion. In this case, the band of interest is the S–N–S symmetric stretching at about 730 cm^{-1}, already used for the quantitative analysis of the DMF/FSI^- ratio. As illustrated in Figure 3d, this band could be fitted by a sum of three Gaussian functions centered at 719, 731, and 739 cm^{-1}. These three peaks correspond to the stretching mode of the anion in the free, contact ion pair (CIP, one FSI^- interacting with one Li^+), and aggregate (AGG, one FSI^- interacting with at least two Li^+) configurations, respectively, and their areas are directly proportional to the respective populations. (44,45) By varying the solute concentration, we obtained different relative populations for the three geometries; see Figure 3d. In diluted conditions ([DMF]/[LiFSI] ≥3 mol/mol) the anion is present in only two configurations: free and contaction pair, whereas at higher concentrations the anion is completely bound, either as contact ion pair or aggregate. For the most concentrated solution, with a concentration very close to that measured in the membrane, the percentage of aggregate ions is 42%, which is slightly higher than the 33% reported for the membrane. The presence of the polymer matrix, therefore, reduces the amount of cations capable of supporting effective charge transport, but still leaves an appreciable amount of Li capable of carrying charge.

3.2.2. DFT Modeling

We performed DFT calculations to gain detailed insight into the interactions of Li^+ with DMF and PVDF. We simulated a Li^+ ion surrounded by an increasing number of solvent DMF molecules and PVDF oligomers, and we evaluated the binding energies of the different complexes. Figure 4a reports the binding energy, Δ*E*, of the different complexes against the number of ligands. The binding energy of DMF with PVDF is weak (on the order of −0.2 eV) and was not reported. We see that Li^+ is significantly more stable, by about 0.3 eV, when it is bound to one DMF molecule compared to when it interacts with a PVDF chain. Similarly, when considering two ligands, the $Li(DMF)_2^+$ complex is more stable than $Li(PVDF)_2^+$. The latter is competitive with complex binding DMF and PVDF, $Li(DMF)(PVDF)^+$. The formation of complexes with DMF only is still more stable with three ligands; see Figure 4a. With four ligands, the energy difference between the complex containing only DMF ligands ($Li(DMF)_4^+$, Figure 4b) and the ones interacting with PVDF, $Li(DMF)_3(PVDF)^+$ (Figure 4c) and $Li(DMF)_2(PVDF)_2^+$ (Figure 4d), becomes smaller as shown by the binding energy in Figure 4a. When the number of ligands is five, we considered $Li(DMF)_n(PVDF)_m^+$ with n = 3–5 and m = 1,2. For all of these configurations, in the optimized structure, only DMF coordinates with Li^+ while PVDF forms a second solvation shell (Figure S7). The resulting configurations, with $Li(DMF)_4^+$ interacting with one PVDF ($Li(DMF)_4(PVDF)^+$) and $Li(DMF)_3^+$ interacting with two PVDF oligomers ($Li(DMF)_3(PVDF)_2^+$), become more stable than the $Li(DMF)_5^+$ complex. When the number of ligands is six, the only stable complex is the $Li(DMF)_6^+$ one, as the PVDF does not coordinate with Li^+ in $Li(DMF)_n(PVDF)_m^+$ with $n + m = 6$ and m = 1–3. These results show that Li^+ tends to coordinate up to three DMF molecules in place of directly binding PVDF, indicating that the interaction Li^+–DMF is stronger than the interaction Li^+–PVDF. Increasing the number of ligands, e.g., $n+m > 4$, the $Li(DMF)_n^+$ complex interacts with PVDF as the second solvation shell.

Figure 4

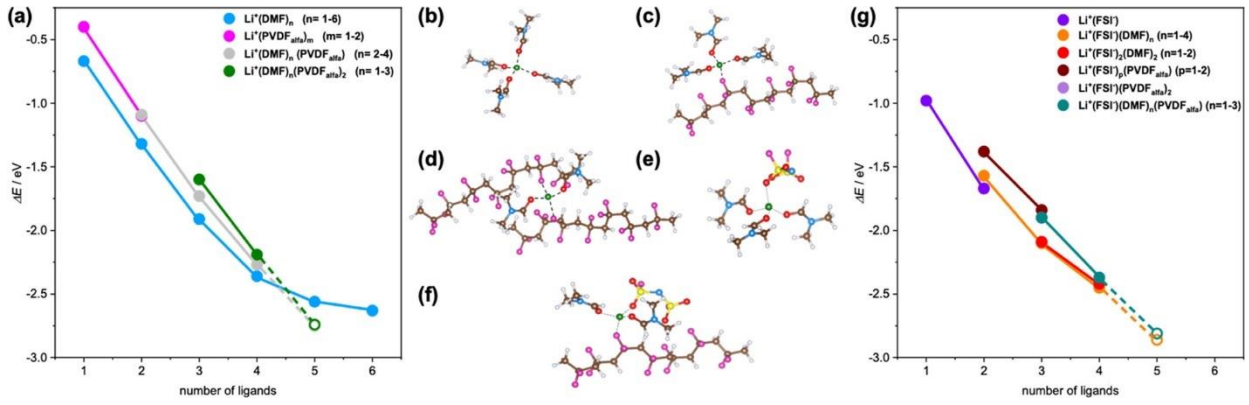

Figure 4. Binding energy (ΔE) and structural properties of $Li(FSI^-)_p(DMF)_n(PVDF)_m^+$ complexes. (a) Binding energy of $Li(DMF)_n(PVDF)_m^+$ complexes as a function of the number of ligands surrounding the lithium cation (n + m). (b–d) Optimized structures of $Li(DMF)_n(PVDF)_m^+$ with n + m = 4: $Li(DMF)_4^+$ (b), $Li(DMF)_3(PVDF)^+$ (c), and $Li(DMF)_2(PVDF)_2^+$ (d). (e–f) Optimized structures of anion-containing complexes: $Li(FSI^-)(DMF)_3^+$ (e), $Li(FSI^-)(DMF)_2(PVDF)^+$ (f). Carbon atoms are represented in brown, nitrogen in light blue, fluorine in magenta, oxygen in red, hydrogen in white, and lithium in green. (g) Binding energy of $Li(FSI^-)_p(DMF)_n(PVDF)_m^+$ complexes as a function of the number of ligands surrounding the lithium cation (p + n + m). Configurations where PVDF and FSI^- relax from the first to the second Li^+ coordination shell during the geometry are represented with a dotted line (see structures in Figure S7 and Table S2).

The analysis was then extended to the interaction of Li^+ with DMF and PVDF in the presence of the FSI^- anions. The binding energies, Δ*E*, of Li^+ complexes in the presence of the FSI^- anion are shown in Figure 4g. The binding energies of the anion with PVDF and DMF are much weaker ($\Delta E > -0.15$ eV for (FSI^-)(DMF) and (FSI^-)(PVDF) complexes) and were not reported. First, we can observe that the interaction of Li^+ with FSI^- is more than 0.3 eV stronger than the single interaction between Li^+ and DMF or PVDF. Considering the $Li(FSI^-)(DMF)^+$ complex, this is more stable than the two-ligand complexes without the anion by 0.25 eV or more. By increasing the number of ligands, e.g., 3, the greater stability of the complexes presenting the anion is markedly reduced. In fact, the $Li(FSI^-)(DMF)(PVDF)^+$ and

$Li^+(FSI^-)(DMF)_2$ complexes turn out to be ca. 0.1 eV more stable than the analogous $Li^+(DMF)_3$ complex. Turning now to the $Li(FSI^-)_p(DMF)_n(PVDF)_m^+$ complexes with four ligands (p = 0–2, n = 1–3 and m = 0–1), the energy difference between complexes with and without anion in the first solvation shell is less than 0.10 eV. Interestingly, with five ligands, the complexes with FSI^- in the second solvation shell become more stable by about 0.25 eV than the corresponding complexes with FSI^- in the first shell, both for $Li(FSI^-)(DMF)_4^+$ and $Li(FSI^-)(DMF)_3(PVDF)^+$ (Table S2).

These results show that Li^+ tends to remain coordinated to its anion when coordinated with a limited number of ligands, but in the presence of more DMF molecules ($n > 3$ in $Li(FSI^-)_p(DMF)_n(PVDF)_m^+$) the interaction with DMF, with the anion localized in the second shell, becomes competitive.

The strong interaction between Li^+ and DMF molecules is further supported by the theoretical simulation of IR and Raman spectra, which show similar trends. The calculated IR and Raman spectra of the optimized structures of a DMF molecule, together with the ones of $Li(DMF)^+$ and $Li(DMF)_3^+$ complexes are reported in Figure 5 bottom panels. A comparison of the spectra for free-DMF and bound-DMF ($Li(DMF)_n^+$) in the O═C–N deformation region (640–690 cm^{-1}) illustrates significant changes in the position of the peak. As observed in the experimental spectra, DMF presents a peak at 660 cm^{-1}, whereas $Li(DMF)^+$ shows a peak at 691 cm^{-1} whose intensity gradually increases with an increasing amount of DMF molecules (Figures 5, S8a, and S9a). Also of interest is the region of C–N–C symmetric stretching at around 871 cm^{-1} which is only Raman active and could be used to estimate the DMF/FSI^- ratio. As for the previous stretching, the intensity of this peak gradually increases from DMF to $Li(DMF)_n^+$ (Figure S9b). Considerable changes due to the coordination with Li^+ can be observed in the CH_3 deformation region, 1000–1200 cm^{-1} (Figures 5, S8b, and S9c). Moreover, in the region of 1700–1760 cm^{-1}, there is the band corresponding to C═O vibrations (stretching), which has a peak at 1756.9 cm^{-1} in our calculations. The C═O peak shifts to 1716.7 cm^{-1} and becomes more intense in the $Li(DMF)_n^+$ complexes, indicating that the formation of the complexes causes a red shift of 40 cm^{-1} (Figures 5, S8c and S9d). Figure 5 middle panels show the computed infrared and Raman spectra of $Li^+(FSI^-)$, $Li^+(FSI^-)(DMF)$, and $Li^+(FSI^-)(DMF)_2$ complexes. These spectra are rather complex, but it is clearly evident that the computed spectra of $Li^+(FSI^-)(DMF)_n$ have all of the characteristic frequencies of $Li^+(FSI^-)$ and $Li(DMF)_n^+$ complexes. The simulated spectra of the optimized structures of the PVDF chain and $Li(PVDF)^+$ complex are reported in Figure 5 top panels. Interestingly, the PVDF and $Li(PVDF)^+$ spectra are overlapping, further confirming that the interaction between Li^+ and the PVDF chain is weak, as it has no effect on the PVDF vibrations.

Figure 5

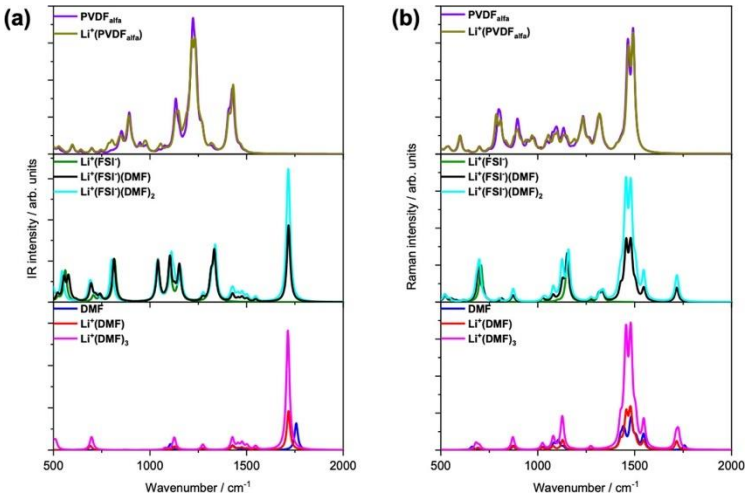

Figure 5. Simulated IR (a) and Raman (b) spectra of $Li(FSI^-)_p(DMF)_n(PVDF)_m^+$ complexes. IR/Raman spectra of (bottom) DMF molecule, $Li(DMF)^+$, and $Li(DMF)_3^+$ complexes; (middle) $Li^+(FSI^-)$ salt, $Li(FSI^-)(DMF)^+$, and $Li(FSI^-)(DMF)_2^+$ complexes; (top) PVDF chain and $Li(PVDF)^+$ complex.

The simulated vibrational spectra show important differences in the region of S–N–S stretching (600–750 cm^{-1}), providing insights into FSI^- coordination. Figure 6a illustrates the stretching mode of $(FSI_{cis}^-)(DMF)_4^+$ complexes (free cases) in three different mediums: PVDF (ε = 10.1), acetone (ε = 20.5), and DMF (ε = 37.2). Complexes containing free FSI_{cis}^- or FSI_{trans}^- are isoenergetic, and therefore the following results were obtained considering only FSI_{cis}^-. It can be observed that the effect due to the medium dielectric constant is negligible, and the peaks are all located at around 680 cm^{-1}. When Li^+ is added to the previous configuration in the presence of an increased number of DMF molecules as shown in Figure 6b (CIP), the peaks shift to around 695 cm^{-1}. In Figure 6c, it is possible to distinguish two different peaks. Interestingly, the position of the S–N–S peak does not depend on the medium, and its shift by about 20 cm^{-1} to higher wavenumbers appears to be independent of the environment.

Figure 6

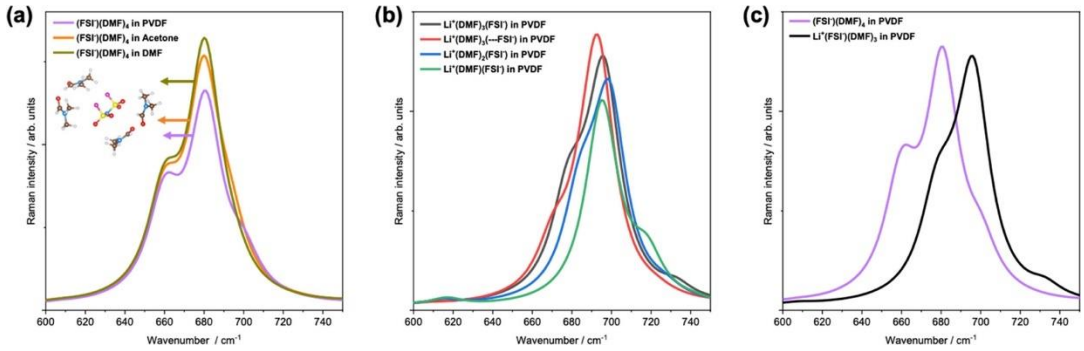

Figure 6. (a) Comparison of Raman spectra of the S–N–S stretching region for $(FSI_{cis}^-)(DMF)_4$ in three different solvents: PVDF (ε = 10.1), acetone (ε = 20.5), and DMF (ε = 37.2). (b) Raman spectra of the S–N–S stretching region for $Li(FSI^-)(DMF)_n^+$ with n = 1–3 in PVDF matrix (ε = 10.1). (c) Raman spectra of the S–N–S stretching region for $Li(FSI^-)(DMF)_3^+$ and $(FSI_{cis}^-)(DMF_4)$ in the PVDF matrix (ε = 10.1).

The overall vibrational spectroscopic features represent further evidence that the interaction of Li^+ with DMF, even in the presence of FSI^- directly bound or in the second shell, is feasible and strong. This is in full agreement with experimental data. Therefore, preferential solvation of Li^+ by DMF can be expected in its mixture with FSI^- so that the primary solvation sheath of Li^+ markedly depends on the experimental amount of DMF molecules available in the membranes.

3.2.3. Time Domain ^1H NMR

Additional information on the presence of solvent and its interaction with the matrix is provided by Time Domain NMR, a technique specifically informative on the mobility of polymer chains. (46) We prepared an NMR tube with 156 mg of E_7:3_S. PVDF-HFP can present semicrystalline structure (47) so we used an NMR sequence containing a refocusing block specifically tailored for quantitative recovery of the signal. We investigated the membrane prepared with E_7:3_S at 60 °C, higher than room temperature, to enhance the mobility contrast while avoiding any solvent loss during the experiment itself. As seen in Figure 7, the sample free induction decay could be fitted with a function composed of a Gaussian contribution associated with the rigid phase, accounting for around 12% of the signal and a slow relaxing component associated with the mobile phase.

Figure 7

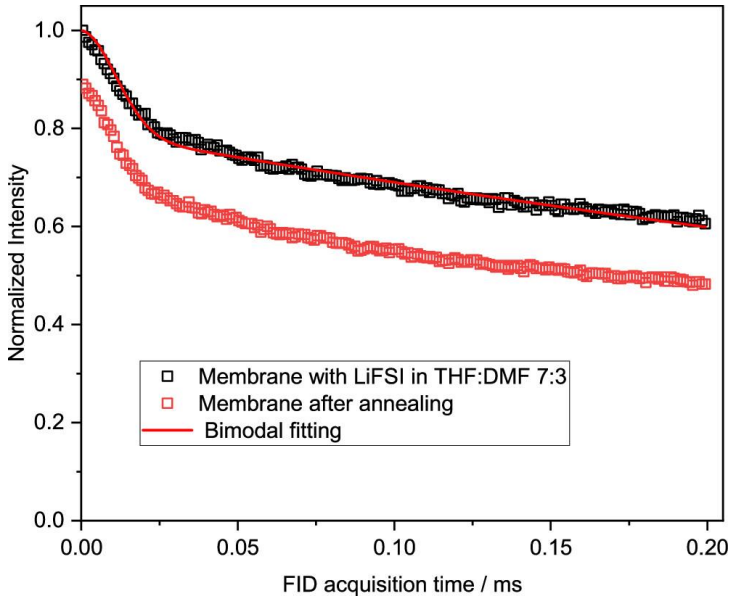

Figure 7. ^1H FID recorded at 60 °C using the MSE pulse sequence of the PVDF-HFP membrane prepared with THF:DMF under the same instrumental conditions. The sample is the same, investigated before and after an overnight annealing at 80 °C. The corresponding spectra are shown in Figure S10.

Repeating the experiment after overnight annealing at 80 °C in an open tube, we noticed both a reduction in the signal intensity and a change in the shape of decay. Since we kept all instrumental conditions, including instrument gain, unchanged, the signal intensity is proportional to the amount of ^1H nuclei in the sample. As seen in Figure 7, where for clarity we normalized all of the data considering the intensity of the pristine sample equal to 1, the loss of intensity is around 11%. The DMF, with 7 H atoms and a molecular weight of 73.09,

has a higher proton content than the highly fluorinated polymer. By considering the different proton content, we estimate that the reduction in ^{1}H signal is associated with the loss of around 4% w/w of residual DMF.

As a result, the rigid fraction of the remaining membrane increases from 12 to 17.5%. This is far more than the simple reproportionation due to the loss of mobile fraction, which means that the DMF removed through annealing also acted as a plasticizer in the material. This measurement supports the hypothesis that, at this composition, a significant part of the DMF is bound to the ions and increases their mobility.

3.3. Ionic Conductivity

Figure 8a shows Arrhenius plots of the ionic conductivity of several samples subjected to different drying processes. The conductivity values decreased as the intensity of the drying treatments increased, i.e., with the decrease in the amount of solvent still available in the QSEs. This is a clear indication of the role played by the solvent in the ion transport mechanism. The conductivity curves showed a Vogel–Tammann–Fulcher (VTF) behavior which is more evident for lower conductivity values. This behavior is typical of polymer systems with significant free volume, or gel-type electrolytes. (21) However, due to the relatively narrow temperature range, the curves could be fitted correctly with the Arrhenius equation. The activation energies were reported in Figure 8: as expected, they increased by decreasing the solvent amount in the matrix. Figure 8b shows the Arrhenius plots of the ionic conductivity of samples dried for 3 days but with initial different amounts of DMF. The membrane prepared using only THF turned out to have a conductivity of $\sim 9 \times 10^{-8}$ S cm^{-1} at room temperature. As the concentration of DMF used as the solvent increases, the electrolytes show higher conductivity throughout the temperature range, with similar activation energy values, confirming that the presence of DMF is necessary to make the material a good ionic conductor. Figure 8c shows the behavior of the ionic conductivity vs the actual amount of DMF in the membranes, as determined by weighing the samples (see Table 1). In terms of site percolation theory, (48) the ionic conductivity can be expressed as

$$\sigma = A(x - x_{tr})^{\alpha} \quad \textbf{(3)}$$

where A is a constant, x is a parameter related to the amount of conducting phase (e.g., its molar fraction), x_{tr} is the threshold value for site percolation, and α is a critical exponent that gives information about the nature and the dimensionality of the network involved in the transport process. By fitting the data of Figure 8c in terms of eq 3, we obtained $x_{tr} \cong 0$ and $\alpha = 1.26$ ($R > 0.99$). A threshold value very close to zero means that pure PVDF (or PVDF-HFP) – LiFSI systems cannot be considered as perfect insulators. In fact, the rt ionic conductivity of the E-THF sample is $\sim 9 \times 10^{-8}$ S cm^{-1}. However, also small quantities of DMF ([DMF]/[Li] = 0.31) lead to a more than 2 orders of magnitude increase of the ionic conductivity ($\sigma = 4.3 \times 10^{-5}$ S cm^{-1}), which confirms that DMF is very effective in determining the formation of a conducting phase. The value of the α exponent slightly higher than 1 points toward a 1D transport mechanism, suggesting a uniform distribution of the DMF among the ordered strands of the semicrystalline polymer matrix.

Figure 8

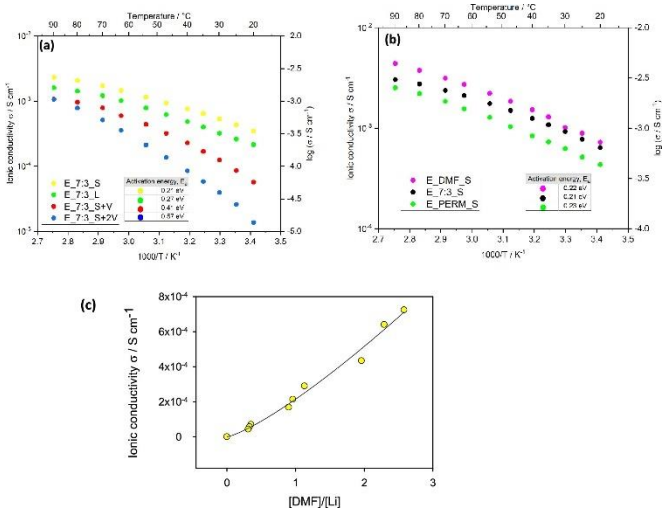

Figure 8. Arrhenius plot of the conductivity of electrolyte membranes: (a) subjected to different drying protocols and (b) with different initial DMF amounts; (c) room-temperature conductivity values vs the DMF amount following different drying protocols (see Table 1c–e). The line is a power law best fit (see text).

Our combined Raman, EIS, and DFT evidence points to a transport mechanism where the Li$^+$ ions are solvated by 2–3 DMF molecules and diffuse among the polymer strands plasticized by the solvent. The forced extraction of DMF leads to a decrease of conductivity and an increase of the activation energy. From elementary physical chemistry, we know that

$$\sigma \propto nu \quad \textbf{(4)}$$

where *n* is the number of carriers and *u* is the mobility. Our Raman results (Figure 3e) suggest that carrier concentration varies almost linearly with the DMF content; therefore, the superlinear behavior observed in Figure 8c must be attributed to the increase of Li^+ mobility due to DMF, which acts both as a plasticizer and as a complexing medium that favors ion transport.

4. Conclusions

In this paper, we discussed the physicochemical properties and the ion transport mechanism in PDVF-based QSEs. In the literature, (8) these very promising systems were claimed to be solid-state electrolytes. Indeed, their robustness and overall mechanical properties well resemble those of solid-state systems. However, we provided circumstantial evidence (9) that a significant amount of residual solvent (e.g., DMF) is entrapped in the polymer matrix and strongly influences the Li^+ transport. Here, our careful DFT modeling, coupled with IR, Raman, and NMR spectroscopies, showed that strong coupling takes place between lithium ions and DMF, whereas the polymer-DMF and polymer-ion interactions are minority. The resulting systems should, therefore, be considered quasi-solid electrolytes, due to the unavoidable and strongly active role played by residual DMF.

The amount of residual, or better permanent, solvent in the polymer matrix is dependent on the drying/aging procedures. However, even prolonged and harsh treatments leave in the matrix quantities of solvent of the order of several weight percent, sufficient to ensure a conductivity close to 10^{-3} ohm^{-1} cm^{-1} at room temperature. From the meso/microstructural point of view, NMR relaxometry measurements highlight that DMF can diffuse in the matrix and act as a plasticizer. Thus, the amount of DMF in the matrix should be carefully tuned to optimize the mechanical and ion diffusion properties relevant to real devices. In a companion paper, we will discuss the electrochemical/functional properties of these systems and how they can be further tuned/improved by the addition of hybrid fillers.

Acknowledgments

This study was carried out within the MOST–Sustainable Mobility Center and received funding from the European Union Next-GenerationEU (PIANO NAZIONALE DI RIPRESA E RESILIENZA (PNRR)–MISSIONE 4 COMPONENTE 2, INVESTIMENTO 1.4-D.D. 1033 17/06/2022, CN00000023). This manuscript reflects only the authors' views and opinions, neither the European Union nor the European Commission can be considered responsible for them. Funding from Italian MUR through the PRIN-2022 project "Self-healing strategies towards next generation lithium rechargeable batteries (HEALIB)" is gratefully acknowledged.

Reference

1. Armand, M.; Tarascon, J.-M. Building Better Batteries. Nature 2008, 451, 652– 657, DOI: 10.1038/451652a
2. Chombo, P. V.; Laoonual, Y. A Review of Safety Strategies of a Li-Ion Battery. J. Power Sources 2020, 478, 228649 DOI: 10.1016/j.jpowsour.2020.228649
3. Li, M.; Wang, C.; Chen, Z.; Xu, K.; Lu, J. New Concepts in Electrolytes. Chem. Rev. 2020, 120, 6783– 6819, DOI: 10.1021/acs.chemrev.9b00531
4. Pasta, M.; Armstrong, D.; Brown, Z. L.; Bu, J.; Castell, M. R.; Chen, P.; Cocks, A.; Corr, S. A.; Cussen, E. J.; Darnbrough, E.; Deshpande, V.; Doerrer, C.; Dyer, M. S.; El-Shinawi, H.; Fleck, N.; Grant, P.; Gregory, G. L.; Grovenor, C.; Hardwick, L. J.; Irvine, J. T. S.; Lee, H. J.; Li, G.; Liberti, E.; McClelland, I.; Monroe, C.; Nellist, P. D.; Shearing, P. R.; Shoko, E.; Song, W.; Jolly, D. S.; Thomas, C. I.; Turrell, S. J.; Vestli, M.; Williams, C. K.; Zhou, Y.; Bruce, P. G. 2020 Roadmap on Solid-State Batteries. J. Phys. Energy 2020, 2 (3), 032008 DOI: 10.1088/2515-7655/ab95f4
5. Quartarone, E.; Mustarelli, P. Review–Emerging Trends in the Design of Electrolytes for Lithium and Post-Lithium Batteries. J. Electrochem. Soc. 2020, 167 (5), 050508 DOI: 10.1149/1945-7111/ab63c4
6. Cheng, X. B.; Zhang, R.; Zhao, C. Z.; Zhang, Q. Toward Safe Lithium Metal Anode in Rechargeable Batteries: A Review. Chem. Rev. 2017, 117 (15), 10403– 10473, DOI: 10.1021/acs.chemrev.7b00115
7. Wang, Q.; Liu, B.; Shen, Y.; Wu, J.; Zhao, Z.; Zhong, C.; Hu, W. Confronting the Challenges in Lithium Anodes for Lithium Metal Batteries. Adv. Sci. 2021, 8 (17), 2101111 DOI: 10.1002/advs.202101111
8. Tikekar, M. D.; Choudhury, S.; Tu, Z.; Archer, L. A. Design Principles for Electrolytes and Interfaces for Stable Lithium-Metal Batteries. Nat. Energy 2016, 1 (9), 16114 DOI: 10.1038/nenergy.2016.114
9. Manthiram, A.; Yu, X.; Wang, S. Lithium Battery Chemistries Enabled by Solid-State Electrolytes. Nat. Rev. Mater. 2017, 2 (4), 16103 DOI: 10.1038/natrevmats.2016.103
10. Zhao, X.; Wang, C.; Liu, H.; Liang, Y.; Fan, L. Z. A Review of Polymer-Based Solid-State Electrolytes for Lithium-Metal Batteries: Structure, Kinetic, Interface Stability, and Application. Batteries Supercaps 2023, 6 (4), e202200502 DOI: 10.1002/batt.202200502
11. Chen, L.; Li, Y.; Li, S. P.; Fan, L. Z.; Nan, C. W.; Goodenough, J. B. PEO/Garnet Composite Electrolytes for Solid-State Lithium Batteries: From "Ceramic-in-Polymer" to "Polymer-in-Ceramic. Nano Energy 2018, 46, 176– 184, DOI: 10.1016/j.nanoen.2017.12.037
12. Wu, L. T.; Nachimuthu, S.; Brandell, D.; Jiang, J. C. Prediction of SEI Formation in All-Solid-State Batteries: Computational Insights from PCL-Based Polymer Electrolyte Decomposition on Lithium-Metal. Batteries Supercaps 2022, 5 (9), e202200088 DOI: 10.1002/batt.202200088
13. Li, Z.; Guo, D.; Li, F.; Hou, G.; Liu, X.; Li, C.; Cao, L.; Wei, R.; Zhou, Z.; Lai, Z. Nerve Network-Inspired Solid Polymer Electrolytes (NN-SPE) for Fast and Single-Ion Lithium Conduction. Energy Storage Mater. 2022, 49, 575– 582, DOI: 10.1016/j.ensm.2022.05.003
14. Quartarone, E.; Mustarelli, P.; Magistris, A. PEO-Based Composite Polymer Electrolytes. Solid State Ionics 1998, 110, 1– 14, DOI: 10.1016/S0167-2738(98)00114-3

15. Jiang, Y.; Yan, X.; Ma, Z.; Mei, P.; Xiao, W.; You, Q.; Zhang, Y. Development of the PEO Based Solid Polymer Electrolytes for All-Solid State Lithium Ion Batteries. Polymers 2018, 10 (11), 1237 DOI: 10.3390/polym10111237
16. Mezzomo, L.; Lorenzi, R.; Mauri, M.; Simonutti, R.; D'Arienzo, M.; Wi, T. U.; Ko, S.; Lee, H. W.; Poggini, L.; Caneschi, A.; Mustarelli, P.; Ruffo, R. Unveiling the Role of PEO-Capped TiO2Nanofiller in Stabilizing the Anode Interface in Lithium Metal Batteries. Nano Lett. 2022, 22 (21), 8509– 8518, DOI: 10.1021/acs.nanolett.2c02973
17. Wu, Y.; Li, Y.; Wang, Y.; Liu, Q.; Chen, Q.; Chen, M. Advances and Prospects of PVDF Based Polymer Electrolytes. J. Energy Chem. 2022, 64, 62– 84, DOI: 10.1016/j.jechem.2021.04.007
18. Zhou, D.; Shanmukaraj, D.; Tkacheva, A.; Armand, M.; Wang, G. Polymer Electrolytes for Lithium-Based Batteries: Advances and Prospects. Chem. 2019, 5 (9), 2326– 2352, DOI: 10.1016/j.chempr.2019.05.009
19. Mouraliraman, D.; Shaji, N.; Praveen, S.; Nanthagopal, M.; Ho, C. W.; Karthik, M. V.; Kim, T.; Lee, C. W. Thermally Stable PVDF-HFP-Based Gel Polymer Electrolytes for High-Performance Lithium-Ion Batteries. Nanomaterials 2022, 12 (7), 1056 DOI: 10.3390/nano12071056
20. Yi, L.; Zou, C.; Chen, X.; Liu, J.; Cao, S.; Tao, X.; Zang, Z.; Liu, L.; Chang, B.; Shen, Y.; Wang, X. One-Step Synthesis of PVDF-HFP/PMMA-ZrO2Gel Polymer Electrolyte to Boost the Performance of a Lithium Metal Battery. ACS Appl. Energy Mater. 2022, 5 (6), 7317– 7327, DOI: 10.1021/acsaem.2c00831
21. Quartarone, E.; Mustarelli, P. Electrolytes for Solid-State Lithium Rechargeable Batteries: Recent Advances and Perspectives. Chem. Soc. Rev. 2011, 40 (5), 2525– 2540, DOI: 10.1039/c0cs00081g
22. Periasamy, P.; Tatsumi, K.; Shikano, M.; Fujieda, T.; Saito, Y.; Sakai, T.; Mizuhata, M.; Kajinami, A.; Deki, S. Studies on PVdF-Based Gel Polymer Electrolytes. J. Power Sources 2000, 88, 269– 273, DOI: 10.1016/S0378-7753(99)00348-1
23. Zhang, X.; Wang, S.; Xue, C.; Xin, C.; Lin, Y.; Shen, Y.; Li, L.; Nan, C. W. Self-Suppression of Lithium Dendrite in All-Solid-State Lithium Metal Batteries with Poly(Vinylidene Difluoride)-Based Solid Electrolytes. Adv. Mater. 2019, 31 (11), 1806082 DOI: 10.1002/adma.201806082
24. Zhang, X.; Han, J.; Niu, X.; Xin, C.; Xue, C.; Wang, S.; Shen, Y.; Zhang, L.; Li, L.; Nan, C. W. High Cycling Stability for Solid-State Li Metal Batteries via Regulating Solvation Effect in Poly(Vinylidene Fluoride)-Based Electrolytes. Batteries Supercaps 2020, 3 (9), 876– 883, DOI: 10.1002/batt.202000081
25. Wang, Y.; Huang, K.; Zhang, P.; Li, H.; Mi, H. PVDF-HFP Based Polymer Electrolytes with High Li+ Transference Number Enhancing the Cycling Performance and Rate Capability of Lithium Metal Batteries. Appl. Surf. Sci. 2022, 574, 151593 DOI: 10.1016/j.apsusc.2021.151593
26. Zhou, S.; Zhong, S.; Dong, Y.; Liu, Z.; Dong, L.; Yuan, B.; Xie, H.; Liu, Y.; Qiao, L.; Han, J.; He, W. Composition and Structure Design of Poly(vinylidene fluoride)-Based Solid Polymer Electrolytes for Lithium Batteries. Adv. Funct. Mater. 2023, 33 (20), 2214432 DOI: 10.1002/adfm.202214432
27. Frisch, M. J.; Trucks, G. W.; Schlegel, H. B.; Scuseria, G. E.; Robb, M. A.; Cheeseman, J. R.; Scalmani, G.; Barone, V.; Petersson, G. A.; Nakatsuji, H.; Li, X.; Caricato, M.; Marenich, A. V.; Bloino, J.; Janesko, B. G.; Gomperts, R.; Mennucci, B.; Hratchian, H. P.; Ortiz, J. V.; Izmaylov, A. F.; Sonnenberg, J. L.; Williams-Young, D.; Ding, F.; Lipparini, F.; Egidi, F.; Goings, J.; Peng, B.; Petrone, A.; Henderson, T.; Ranasinghe, D.; Zakrzewski, V. G.; Gao, J.; Rega, N.; Zheng, G.; Liang, W.; Hada, M.; Ehara, M.; Toyota, K.; Fukuda, R.; Hasegawa, J.; Ishida, M.; Nakajima, T.; Honda, Y.; Kitao, O.; Nakai, H.; Vreven, T.; Throssell, K.; Montgomery, J. A., Jr.; Peralta, J. E.; Ogliaro, F.; Bearpark, M. J.; Heyd, J. J.; Brothers, E. N.; Kudin, K. N.; Staroverov, V. N.; Keith, T. A.; Kobayashi, R.; Normand, J.; Raghavachari, K.; Rendell, A. P.; Burant, J. C.; Iyengar, S. S.; Tomasi, J.; Cossi, M.; Millam, J. M.; Klene, M.; Adamo, C.; Cammi, R.; Ochterski, J. W.; Martin, R. L.; Morokuma, K.; Farkas, O.; Foresman, J. B.; Fox, D. J. Gaussian 16; Revision C.01; Gaussian, Inc.: Wallingford, CT, 2016.
28. Cossi, M.; Rega, N.; Scalmani, G.; Barone, V. Energies, Structures, and Electronic Properties of Molecules in Solution with the C-PCM Solvation Model. J. Comput. Chem. 2003, 24 (6), 669– 681, DOI: 10.1002/jcc.10189
29. Tomasi, J.; Mennucci, B.; Cammi, R. Quantum Mechanical Continuum Solvation Models. Chem. Rev. 2005, 105 (8), 2999– 3093, DOI: 10.1021/cr9904009
30. Schaftenaar, G.; Noordik, J. H. Molden: A Pre-and Post-Processing Program for Molecular and Electronic Structures*. J. Comput. Aided Mol. Des. 2000, 14, 123– 134, DOI: 10.1023/A:1008193805436
31. Zhang, X.; Wang, S.; Xue, C.; Xin, C.; Lin, Y.; Shen, Y.; Li, L.; Nan, C. W. Response to Comment on "Self-Suppression of Lithium Dendrite in All-Solid-State Lithium Metal Batteries with Poly(Vinylidene Difluoride)-Based Solid Electrolytes. Adv. Mater. 2020, 32 (14), 2000026 DOI: 10.1002/adma.202000026
32. Callegari, D.; Bonizzoni, S.; Berbenni, V.; Quartarone, E.; Mustarelli, P. Is It Possible to Obtain Solvent-Free, Li+-Conducting Solid Electrolytes Based on Pure PVdF? Comment on "Self-Suppression of Lithium Dendrite in All-Solid-State Lithium Metal Batteries with Poly(Vinylidene Difluoride)-Based Solid Electrolytes. Adv. Mater. 2020, 32 (14), 1907375 DOI: 10.1002/adma.201907375
33. Kerner, M.; Plylahan, N.; Scheers, J.; Johansson, P. Thermal Stability and Decomposition of Lithium Bis(Fluorosulfonyl)Imide (LiFSI) Salts. RSC Adv. 2016, 6 (28), 23327– 23334, DOI: 10.1039/C5RA25048J
34. Han, H.-B.; Zhou, S.-S.; Zhang, D.-J.; Feng, S.-W.; Li, L.-F.; Liu, K.; Feng, W.-F.; Nie, J.; Li, H.; Huang, X.-J.; Armand, M.; Zhou, Z.-B. Lithium Bis(Fluorosulfonyl)Imide (LiFSI) as Conducting Salt for Nonaqueous Liquid Electrolytes for Lithium-Ion Batteries: Physicochemical and Electrochemical Properties. J. Power Sources 2011, 196 (7), 3623– 3632, DOI: 10.1016/j.jpowsour.2010.12.040
35. Shurvell, H. F.; Southby, M. C. Vibrational Spectroscopy Infrared and Raman Spectra of Tetrahydrofuran Hydroperoxide. Vib. Spectrosc. 1997, 15, 137– 146, DOI: 10.1016/S0924-2031(97)00031-3
36. Paschoal, V. H.; Faria, L. F. O.; Ribeiro, M. C. C. Vibrational Spectroscopy of Ionic Liquids. Chem. Rev. 2017, 117 (10), 7053– 7112, DOI: 10.1021/acs.chemrev.6b00461

37. Hushvaktov, H.; Jumabaev, A.; Doroshenko, I.; Absanov, A. Raman Spectra and Non-Empirical Calculations of Dimethylformamide Molecular Clusters Structure. Vib. Spectrosc. 2021, 117, 103315 DOI: 10.1016/j.vibspec.2021.103315
38. Maier, M.; Abbas, D.; Komma, M.; Solihul Mu'min, M.; Thiele, S.; Böhm, T. A Comprehensive Study on the Ionomer Properties of PFSA Membranes with Confocal Raman Microscopy. J. Membr. Sci. 2023, 669, 121244 DOI: 10.1016/j.memsci.2022.121244
39. Ståkhandske, C. M. V.; Mink, J.; Sandstrism, M.; Pfipai, I.; Johansson, P. Vibrational Spectroscopic and Force Field Studies of N,N-Dimethylthioformamide, N,N-Dimethylformamide, Their Deuterated Analogues and Bis(N, N-Dimethylthioformamide) Mercury(II) Perchlorate. Vib. Spectrosc. 1997, 14, 207– 227, DOI: 10.1016/S0924-2031(97)00003-9
40. Sawyer, J. F.; Schrobilgen, G. J.; Sutherland, S. J. Crystal Structure, Raman, and Multinuclear Magnetic Resonance Study of FXeN(S02F)2, an Example of Xenon-Nitrogen Bonding. Inorg. Chem. 1982, 21, 4064– 4072, DOI: 10.1021/ic00141a037
41. James, D. W.; Mayes, R. E.; Leong, H.; Jamie, I. M.; Zhens, G. Solvation and Ion Association in Solutions Containing Oxyanions. Faraday Discuss. Chem. Soc. 1988, 85, 269– 281, DOI: 10.1039/dc9888500269
42. Umebayashi, Y.; Matsumoto, K.; Mekata, I.; Ishiguro, S.-I. Solvation Structure of Lanthanide(III) Ions in Solvent Mixtures of N,N-Dimethylformamide and N,N-Dimethylacetamide Studied by Titration Raman Spectroscopyy. Phys. Chem. Chem. Phys. 2002, 4, 5599–5605, DOI: 10.1039/b204162f
43. Fujii, K.; Wakamatsu, H.; Todorov, Y.; Yoshimoto, N.; Morita, M. Structural and Electrochemical Properties of Li Ion Solvation Complexes in the Salt-Concentrated Electrolytes Using an Aprotic Donor Solvent, N,N-Dimethylformamide. J. Phys. Chem. C 2016, 120 (31), 17196– 17204, DOI: 10.1021/acs.jpcc.6b04542
44. Stigliano, P.; Ferrara, C.; Pianta, N.; Gentile, A.; Mezzomo, L.; Lorenzi, R.; Berbenni, V.; Ruffo, R.; Battista Appetecchi, G.; Mustarelli, P. Physicochemical Properties of Pyr13 TFSI-NaTFSI Electrolyte for Sodium Batteries. Electrochim. Acta 2022, 412, 140123 DOI: 10.1016/j.electacta.2022.140123
45. Lassègues, J.-C.; Grondin, J.; Talaga, D. Lithium Solvation in Bis (Trifluoromethanesulfonyl) Imide-Based Ionic Liquids. Phys. Chem. Chem. Phys. 2006, 8, 5629– 5632, DOI: 10.1039/B615127B
46. Besghini, D.; Mauri, M.; Simonutti, R. Time Domain NMR in Polymer Science: From the Laboratory to the Industry. Appl. Sci. 2019, 9 (9), 1801, DOI: 10.3390/app9091801
47. Abbrent, S.; Plestil, J.; Hlavata, D.; Lindgren, J.; Tegenfeldt, J.; Wendsjö, Å. Crystallinity and Morphology of PVdF-HFP-Based Gel Electrolytes. Polymer 2001, 42, 1407– 1416, DOI: 10.1016/S0032-3861(00)00517-6
48. Sahimi, M. Applications of Percolation Theory, 2nd ed.; Springer, 2023.